SDI+: A Novel Algorithm for Segmenting Dermoscopic Images

Mario Rosario Guarracino and Lucia Maddalena, *Member, IEEE*

***Abstract*—Malignant skin lesions are among the most common types of cancer, and automated systems for their early detection are of fundamental importance. We propose SDI+, an unsupervised algorithm for the segmentation of skin lesions in dermoscopic images. It is articulated into three steps, aimed at extracting preliminary information on possible confounding factors, accurately segmenting the lesion, and post-processing the result. The overall method achieves high accuracy on dark skin lesions and can handle several cases where confounding factors could inhibit a clear understanding by a human operator. We present extensive experimental results and comparisons achieved by the SDI+ algorithm on the ISIC 2017 dataset, highlighting the advantages and disadvantages.**

***Index Terms*—Dermoscopic image, pre-processing of artifacts, skin lesion segmentation.**

I. Introduction

IN MANY countries, malignant skin lesions are among the most common types of cancer. In the United States, the number of new cases per year is higher than the incidence of breast, prostate, lung, and colon cancers together [1]. In Australia, melanoma is the third most common cancer in men, and it is accounted for 12% of all new tumors diagnosed in 2017 [2]. Higher incidence rates have been observed in New Zealand, with 50 cases per 100.000 people each year, compared to Australia (48 per 100.000), US (21.6 per 100.000 in 2012), and Europe (13.2 per 100.000) [3]. The first therapy approved by US Food and Drug Administration for melanoma lesions was introduced in 2015 and proved to decrease lesions in only 16.3% of treated patients.[1] Currently, the only other available options are surgery and radiotherapy. Therefore, prevention and early detection remain the only possible ways to reduce the incidence and mortality associated with these types of cancer.

Several diagnostic protocols are usually adopted by dermatologists to analyze and classify skin lesions, such as the so-called *ABCD rule* of dermoscopy [4]. Due to the subjective nature of the examination, the accuracy of diagnosis heavily depends on human vision and dermatologist expertise. Computerized dermoscopic image analysis systems, based on the extraction and analysis of domain-specific image features, do not have the limitation of this subjectivity. These systems involve the use of computerized analysis as a second independent and objective diagnostic method, which can enable a pre-screening of patients performed by non-experienced operators. Although image analysis techniques cannot provide a definitive diagnosis, they can improve biopsy decision-making, which some observers feel is the most important use for dermoscopy [5], [6]. Until recently, numerous articles proposed systems for the automated detection of malignant melanoma in skin lesions (e.g., [7]–[15]). The ISIC 2017 Challenge [16] provided a strong stimulus to the topic, soliciting numerous groups to compete for achieving high accuracy in skin lesion segmentation. In this context, we introduced an automatic algorithm [17], named SDI, for the segmentation of skin lesions in dermoscopic images, articulated into three main steps: selection of the image region of interest (ROI), selection of the segmentation band, and segmentation.

Here, we propose an enhancement of the SDI algorithm, referred to as SDI+ algorithm in the following, which provides *i)* an automatic unsupervised method for segmenting dark skin lesions in dermoscopic images, *ii)* new pre-processing and segmentation capabilities, and *iii)* low execution times. Further contributions include the public availability of the source code and a detailed analysis of the ISIC 2017 dataset ground truths.

The paper is organized as follows. In Section II, we describe the SDI+ algorithm, detailing its main steps. In Section III, we provide a thorough quantitative and qualitative analysis of experimental results on the ISIC 2017 dataset [16], also discussing advantages and disadvantages. Finally, discussions and conclusions are drawn in Section IV.

II. Method

The objective of the SDI+ algorithm is to segment dark skin lesions in dermoscopic images. It consists of three consecutive main steps: pre-processing, segmentation, and post-processing. Pre-processing extracts information about the dermoscopic image content, including dark regions, hair, and specular highlights, which deserve specific treatment in the segmentation step. The core step is segmentation, which selects an initial binary mask representing the location of the lesion in the dermoscopic image. Post-processing refines the obtained mask, to

Manuscript received October 31, 2017; revised January 22, 2018; accepted February 17, 2018. Date of publication February 23, 2018; date of current version March 6, 2019. The work of M. R. Guarracino was supported by the RSF under Grant 14-41-00039. The work of L. Maddalena was supported by the Interomics Italian Flagship Project. *(Corresponding author: Lucia Maddalena.)*

The authors are with the National Research Council, Institute for High-Performance Computing and Networking, Naples 80131, Italy (e-mail: mario.guarracino@cnr.it; lucia.maddalena@cnr.it).

Digital Object Identifier 10.1109/JBHI.2018.2808970

[1]https://www.aimatmelanoma.org/melanoma-treatment-options/fda-approved-drugs-for-melanoma/

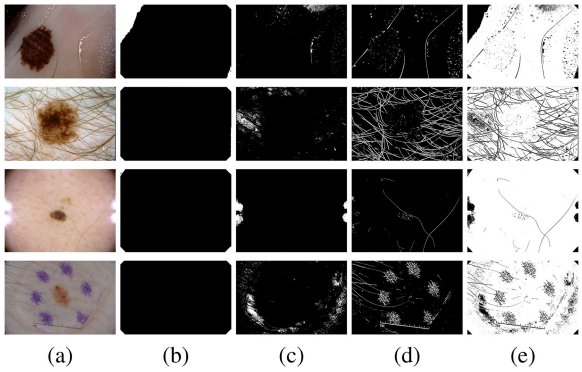

Fig. 1. Preliminary information extraction: ISIC dataset images 15309, 15476, 14590, and 16044 (a) and their masks of dark areas (b), highlights (c), hair (d), and ROI (e).

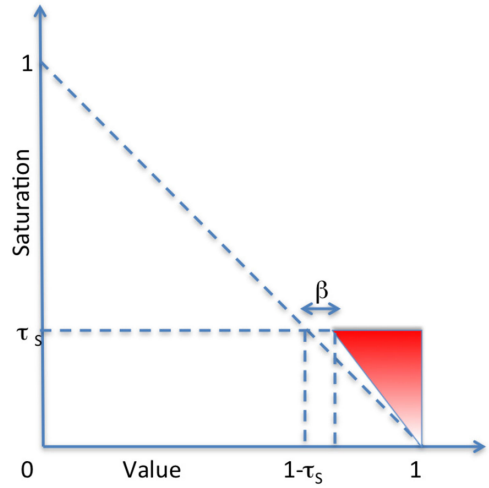

Fig. 2. VS diagram and its region (in red) for detecting highlights.

better conform it to what is manually selected as lesion area by an expert dermatologist.

A. Preliminary Information Extraction

The first step of the SDI+ algorithm selects the ROI, i.e., the subset of image pixels that belong to either the lesion or the skin. This region excludes image pixels belonging to *i)* dark areas of the image border and corners, *ii)* specular highlights, and *iii)* hair. These areas will be adequately taken into account in the subsequent steps of the algorithm, leading to a more accurate segmentation of the skin lesion.

Dark areas include image borders which do not contain the patient's skin, as well as image corners that are often much darker than the image center. They are detected choosing, in the Value band of the image in the HSV color space [18], pixels that are darker than a predefined threshold τ_D. These pixels are selected if they cover most of the border or the corner areas of the image. Fig. 1(b) shows examples of detected dark areas. Here, they are represented through binary masks of the same size of the input image, where pixels belonging to dark areas are set to one (white), while all the other pixels are set to zero (black).

Highlights are bright spots in an image that typically appear in regions with specular reflectance [19]. They are a significant obstacle for proper feature extraction, producing visual features different from those of their neighborhood and, in extreme cases, causing loss of the underlying information. Many methods attempt to separate the diffuse and specular reflection components [20], while others exploit the characterization of highlights in terms of local coincidence of intense brightness and low color saturation [21], [22]. Based on the latter approaches, we detect highlights as image pixels located in the bottom right region of the VS diagram, where V represents the intensity and S the saturation of the pixels in the HSV color space. Specifically, we propose to detect image pixels as highlights if:

$$(S \geq \tau_S) \wedge \left(V \geq 1 + S\frac{\beta - \tau_S}{\tau_S}\right)$$

where τ_S and β parameters are described in Fig. 2.

Fig. 1(c) provides examples of detected highlight areas.

Many accurate methods for hair detection have been proposed in literature [23]–[29]. Following [24], we adopt a bottom-hat filter $T_{s_{bh}}(\cdot)$ in the red band R of the RGB image

$$T_{s_{bh}}(R) = R \bullet s_{bh} - R,$$

where s_{bh} is a gray-scale structuring element and $\bullet$ indicates the closing operation. This filter returns an image that contains elements having size smaller than s_{bh} and that are darker than their neighborhood. Fig. 1(d) provides examples of detected hair areas. Here, we observe that the bottom-hat filter allows detecting also portions of other artifacts frequently seen in dermoscopic images [29], such as ruler marks and marker ink signs [e.g., Fig. 1(d), last row], which survive the bottom-hat filtering.

Finally, the complement of the union of the three above masks produces the ROI mask. The last column of Fig. 1 gives examples of ROI masks, where pixels belonging to either the skin or the lesion are set to white, whereas pixels to be adequately treated in subsequent computations are set to black.

This step enhances the analogous step of the SDI algorithm in that it also considers specular highlights and it maintains separately the various masks, to properly treat them in the subsequent segmentation.

B. Segmentation

The segmentation of skin lesions can be carried out based on different image features [29]. Lesion segmentation can be made easier if the proper color band of the dermoscopic image is chosen [30], [31]. In [17], two color bands showed to be particularly suited for the problem: the red band in the normalized RGB color space and the complement of the value band of the image in the HSV color space, in the following referred to as *Rnorm* and *Vcompl*, respectively. Differently from [17], to provide an automatic means for selecting the best segmentation band for each dermoscopy image, SDI+ performs the segmentation of both *Rnorm* and *Vcompl*, postponing the decision based on the obtained results.

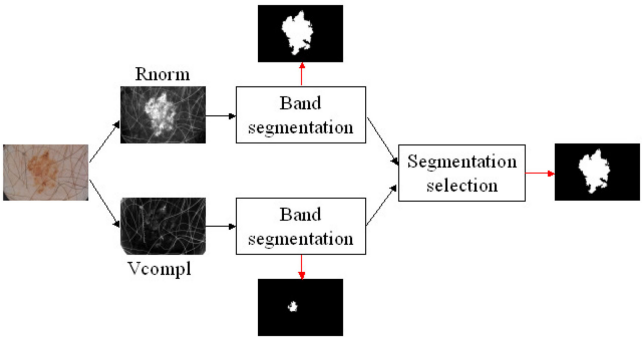

Fig. 3. Block diagram of the SDI+ segmentation step.

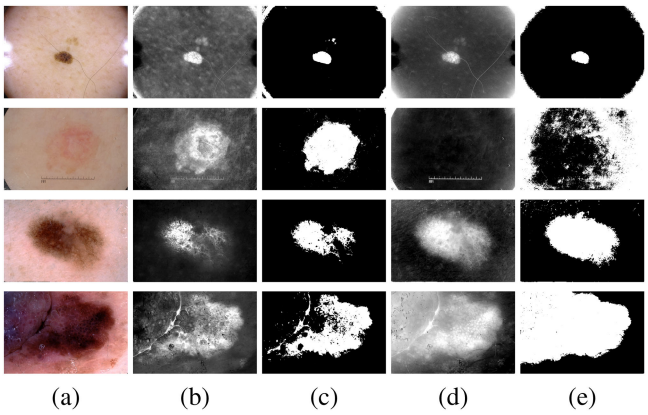

Fig. 4. *Rnorm* and *Vcompl* bands for segmenting dermoscopic images: (a) ISIC dataset images 14590, 14500, 14725, and 14784; (b) *Rnorm*; (c) binarization of *Rnorm*; (d) *Vcompl*; (e) binarization of *Vcompl*.

The block diagram of the segmentation step is shown in Fig. 3 and further details are given in the following sections.

1) Rnorm and Vcompl: The red band in the normalized RGB color space is defined as

$$Rnorm = \frac{R}{R+G+B},$$

where R, G, and B indicate the RGB color bands and the normalization is obtained element-wise for each image pixel. The value band of the HSV color space is defined as

$$V = \max\left(\frac{R}{L}, \frac{G}{L}, \frac{B}{L}\right)$$

where L is the maximum number of gray levels (e.g., $L = 255$ in the usual case of 8-bit images). Instead of the value band V, its complement $Vcompl = 1 - V$ is here adopted for simplicity, since in both the *Rnorm* and *Vcompl* cases a dark lesion appears as a bright image area (e.g., Fig. 4).[2]

Rnorm is often a good choice for segmenting dermoscopic images, as the normalized RGB space eliminates the effect of varying intensities due to uneven illumination and it is free from shadow and shading effects. For example, for the image in the first row of Fig. 4, *Rnorm* is only partially affected by the uneven illumination of the image (darker towards the corners), and its binarization provides a faithful lesion segmentation. Instead, the binarization of *Vcompl* includes also vast skin areas in the image corners, due to their lower illumination. Moreover, in the frequent case of lesions having pink color very similar to the skin color [e.g., second row of Fig. 4], *Rnorm* can be quite helpful in segmenting the lesion, whereas *Vcompl* binarization can produce completely wrong results.

Nevertheless, there are cases where *Vcompl* is a better choice, as shown in the last two rows of Fig. 4. Here, *Rnorm* has lower contrast between some parts of the lesion and the surrounding skin, leading to a partially wrong segmentation, while *Vcompl* binarization provides a much better result.

[2]Note that in Figs. 4, 5, 6, 10, and 12, *Rnorm* and *Vcompl* have been normalized to their maximum value, for display purposes.

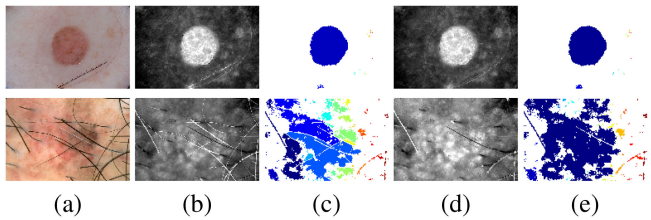

Fig. 5. Band segmentation: (a) ISIC dataset images 15957 and 15004; (b) *Rnorm*; (c) CCs in the segmentation of (b); (d) *Rnorm* with inpainted hair and highlights; (e) CCs in the segmentation of (d).

2) Band Segmentation: In the SDI algorithm [17], band segmentation in the ROI region is obtained by the Otsu algorithm [32], that computes the optimal threshold separating the two classes of pixels (skin and lesion) so that their intra-class variance is minimal. Examples are reported in Fig. 5, showing the *Rnorm* band [Fig. 5(b)] and the connected components (CCs) of its segmentation [Fig. 5(c), where each color corresponds to a different CC].

The presence of hair and highlights, which usually appear close or superimposed to the lesion, can lead to artifacts in the segmented results [e.g., the over-segmentation shown in the second row of Fig. 5(c)]. Therefore, in SDI+ we preliminarily inpaint hair and highlights to reduce these artifacts. Indeed, even though these confounding factors are not perfectly removed by inpainting [Fig. 5(d)], their influence on segmentation is strongly reduced [Fig. 5(e)].

Band segmentation in SDI+ is illustrated through the example provided in Fig. 6. In this case, inpainting in *Rnorm* [Fig. 6(d)] enables an almost perfect lesion segmentation [Fig. 6(e)]. In *Vcompl* [Fig. 6(f)], inpainting manages to remove the ruler mark and isolated hair [Fig. 6(g)]. However, it fails to remove the ink marker signs [as they are only partially included into the hair mask, shown in Fig. 6(b)], that are wrongly included into the segmented image [Fig. 6(h)].

Post-processing of the segmented image is useful in order to select the lesion region among the possible candidate areas, due to image noise and artifacts. Morphological operations for eliminating isolated pixels, closing, and filling areas help reducing artifacts, as shown in Fig. 6(i).

Then, SDI+ computes the connected components found in the resulting segmentation [Fig. 6(j)] and ranks them based on their extension and position. Indeed, as dermoscopic images mainly

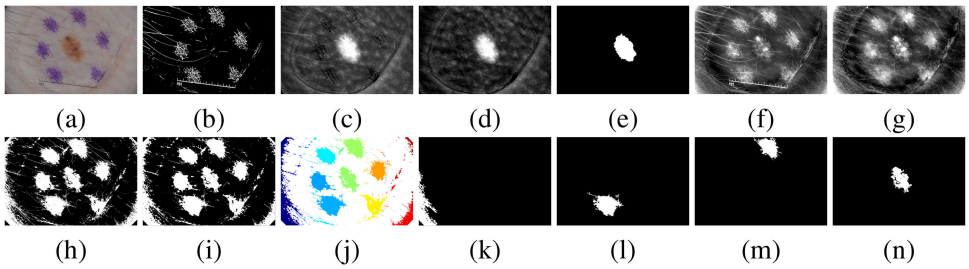

Fig. 6. Band segmentation: (a) ISIC dataset image 16044; (b) hair mask; (c) *Rnorm* band; (d) hair inpainting in *Rnorm* and (e) its segmentation; (f) *Vcompl* band; (g) hair inpainting in *Vcompl* and (h) its segmentation; (i) morphological closing and filling-in of (h); (j) CCs in (i); (k) first CC in (j) ($A = 22568$, $d_C = 506.54$); (l) second CC ($A = 21359$, $d_C = 218.48$); (m) third CC ($A = 16302$, $d_C = 266.34$); (n) fourth CC ($A = 15808$, $d_C = 19.76$).

frame the lesion to be analyzed, generally it appears as the predominant object over the patient skin, positioned around the center of the image. Therefore, possible lesions can be sought among CCs having extended area (number of pixels) and centroid close to the image center. The best lesion candidate is chosen by averaging the rankings of all detected CCs based on area and position. For example, the first four CCs of *Vcompl* segmentation ordered by area A are shown in Fig. 6(k)–(n), also reporting their values of centroid distance d_C from the image center. The CC selected as lesion candidate [Fig. 6(n)] is the fourth (on a total of 12 CCs) in terms of area and the closest to the image center.

3) Segmentation Selection: Once the best lesion candidates have been computed in both *Rnorm* and *Vcompl*, the best segmentation among the two is chosen according to their distance to the image center, solidity, and relative contrast against the skin background. Indeed, besides being centered in the dermoscopic images, skin lesions are usually quite solid as compared to possible confounding factors. Furthermore, contrast against the skin background is higher in the band best suited for segmentation. As an example, for the image of Fig. 6, the only CC detected in *Rnorm* segmentation [Fig. 6(e)] has contrast $c = 5.71$, distance $d_C = 17.97$, and solidity $S = 0.89$, while the one chosen in *Vcompl* [Fig. 6(n)] has $c = 1.50$, $d_C = 19.76$, $S = 0.70$. Therefore, the selected segmentation is the one coming from *Rnorm*, having higher contrast, higher solidity, and lower d_C. Here, the solidity S of a CC is computed as the ratio of its area and the area of its convex hull, while its contrast c is computed as the Weber contrast [33]. These features are computed using only ROI pixel values (i.e., excluding the values of pixels covered not only by dark areas but also by highlights and hair). This strategy prevents any inpainted value from adversely influencing the choice of the best segmentation band. This, in turn, relieves the need for highly accurate, but computationally demanding, hair and highlights inpainting methods for band segmentation (see Section II-B2).

C. Post-Processing

Morphological dilation is applied to the initial segmentation produced in the previous step. Then, the smallest convex set including all its pixels is adopted as final segmentation result. Indeed, even when the initial segmentation well highlights the lesion contour, its convex hull usually better conforms to the ground truth provided by the dermatologist, as exemplified in Fig. 7.

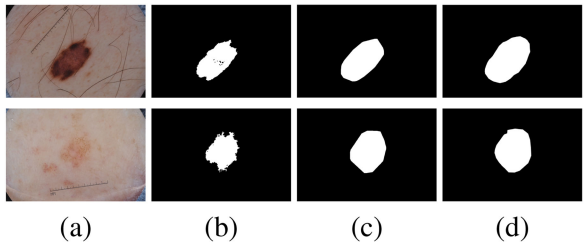

Fig. 7. Post-Processing vs. ground truth: (a) ISIC dataset images 12092 and 14270; (b) segmented lesion; (c) post-processed result; (d) ground truth.

III. Experimental Results and Discussion

A. Implementation Details

An implementation of the SDI+ algorithm in Matlab is made available for future comparisons [34]. Here, any dermoscopic image is resized to have width no greater than 1024 pixels. A fixed set of parameter values has been adopted for all the images, experimentally chosen as follows: threshold $\tau_D = 0.2$ for selecting dark areas, $\tau_S = 0.1$ and $\beta = 0.01$ for detecting highlights, disk of size 5 as structuring element s_{bh} for detecting hair (see Section II-A), and squares of size 3 and 7 as structuring elements for post-processing the initial segmentation (see Section II-B2) and the final segmentation (see Section II-C), respectively. Moreover, inpainting of highlights and hair is obtained through the `regionfill` Matlab function, that smoothly interpolates inward from the pixel values on the boundary of the selected areas by solving Laplace's equation. Inpainting is performed only if hair and highlights occupy no more than 0.1% of the image, to avoid introducing spurious values. Finally, CCs having area smaller than 1200 pixels are not included into the set of possible lesion candidates (see Section II-B2).

B. Data and Ground Truth

The test dataset for the ISIC 2017 lesion segmentation task (here named ISIC dataset for simplicity) consists of 600 dermoscopic images that include skin lesions of different types [16].

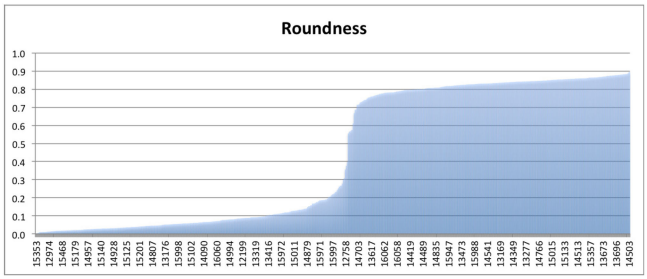

Fig. 8. Roundness of the ground truths of the ISIC dataset. Labels on the x axis indicate the indices of selected images.

Fig. 9. Three ground truths of the ISIC dataset and their roundness values.

Almost all images depict single lesions having more or less uniform dark color, and thus perfectly fit the assumptions made in the design of the SDI+ algorithm. Only six images show lesions that are clearer than the surrounding skin, and 31 images contain either more than one lesion or lesions having non-uniform color, that might be perceived as multiple lesions.

The ground truth (GT) images are given as binary masks having the same size of the corresponding dermoscopic image, where white pixels are considered inside the lesion area, and black pixels are considered outside it. Examining the GT images, it can be observed that, apart from at least six of them that are ambiguous in the shape they delineate, about 50% of the remaining GTs provide very detailed lesion contours (as an automatic segmentation software would do), while the others provide quite rough lesion contours (as a dermatologist would manually do). The smoothness of the lesion contour can be quantified through the *roundness* (also known as *compactness* or *thinness ratio*), defined as [35]

$$Roundness = \frac{4\pi A}{p^2},$$

where A is the lesion area and p its perimeter. Roundness takes values in [0, 1], with 1 being the roundness of a circle and lower values being the roundness of more irregular shapes. Fig. 8 plots roundness values for the ISIC dataset GTs and Fig. 9 reports examples of GT images together with their roundness value.

C. Quantitative Analysis

Performance metrics adopted for evaluating SDI+ are pixel-level accuracy (AC), sensitivity (SE), and specificity (SP), as well as Dice coefficient (DI) and Jaccard index (JA), as defined in [36].

To compare results with all those submitted to the ISIC 2017 Challenge, Table I reports the performance values achieved by SDI and SDI+ on the whole ISIC dataset, as well as those of CDNN [37], the method which, to date, achieved the best performance. It can be observed that SDI+ substantially improves

TABLE I
AVERAGE PERFORMANCE RESULTS ON THE ISIC DATASET

	AC	SE	SP	DI	JA
SDI	0.857	0.692	0.937	0.697	0.592
SDI+	0.888	0.813	0.927	0.782	0.692
CDNN [37]	0.934	0.825	0.975	0.849	0.765

TABLE II
AVERAGE SDI+ PERFORMANCE RESULTS ON SELECTED SUBSETS OF ISIC DATASET

	AC	SE	SP	DI	JA
Ambiguous (6)	0.648	0.554	0.784	0.465	0.352
Non-Uniform (31)	0.772	0.501	0.936	0.490	0.388
Clear (6)	0.651	0.696	0.672	0.657	0.507
Round (259)	0.839	0.765	0.886	0.727	0.623
Sharp (298)	0.952	0.895	0.970	0.870	0.794

TABLE III
AVERAGE EXECUTION TIMES (SECS), INCLUDING I/O, VARYING THE IMAGE RESOLUTION

639×602	2304×1536	3008×2000	4288×2848	6748×4439
2.0	2.8	2.9	3.6	5.1

the performance of SDI in terms of all the considered metrics, however still performing worse than the compared best method.

To gain further insight into the performance results, we partitioned the ISIC dataset into five groups [34], based on the observations on images and related GTs made in Section III-B:

1) *Clear*: 6 images that include lesions that are brighter than the surrounding skin;
2) *Non-Uniform*: 31 images that contain either more than one lesion or lesions having non-uniform color, easily perceived as multiple lesions;
3) *Ambiguous*: 6 images whose GT is ambiguous in the shape it delineates;
4) *Round*: 259 images whose GT provides rough lesion contours, having roundness higher than 0.5;
5) *Sharp*: 298 images whose GT provides precise lesion contour, having roundness no higher than 0.5.

Table II reports average performance results achieved by SDI+ in each group of images. Performances are obviously quite low in those cases (*Clear* and *Non-Uniform*, besides *Ambiguous*) violating the assumptions made in the design of the SDI+ algorithm, whose objective is the segmentation of single lesions having more or less uniform dark color. However, performance is not extremely low for the *Clear* class. This happens because most of the bright lesions have slightly darker borders, which succeed to be segmented. SDI+ could be modified to detect lesions that are clear, rather than dark, by adopting the complement of the *Rnorm* and *Vcompl* segmentation bands. Handling lesions having non-uniform color, instead, would require an adequate mechanism to combine the segmentations of clear and dark lesions, both for band segmentation (Section II-B2) and for segmentation selection (Section II-B3). Analogously, the

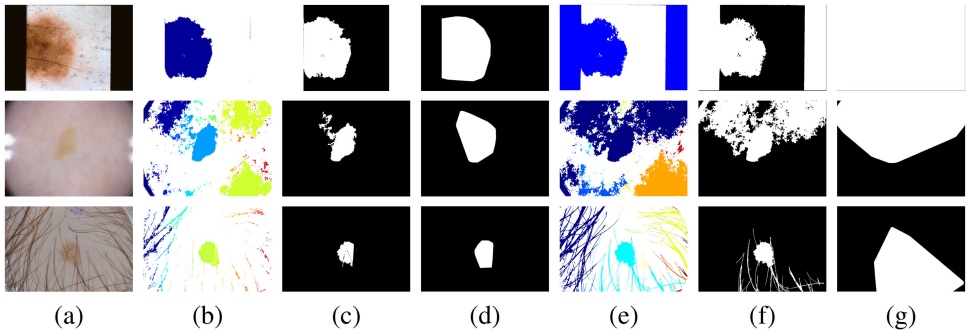

Fig. 10. Need for preliminary information extraction: results obtained by separately treating dark areas, highlights, and hair ((b)–(d)) or not ((e)–(g)). (a): ISIC dataset images 15566, 14575, and 13399; (b) and (e): CCs of the selected band; (c) and (f): selected CC; (d) and (g): final SDI+ segmentation.

method could be generalized to handle multiple lesions by allowing for multiple lesion candidates in both these tasks, and by devising an automatic criterion to discern if there is more than one lesion.

Table II also shows that SDI+ reaches quite high performance for the *Sharp* class, proving that it very well competes with the automatic tool adopted by the dermatologist to label these images, whereas lower values are obtained for the images of the *Round* class. The latter observation suggests that further work on the post-processing step (Section II-C) should be done, to better resemble the manual segmentation provided by the dermatologist.

To complete our quantitative evaluation, in Table III we report SDI+ execution times (in seconds), for different image resolutions. Timings have been obtained by the Matlab implementation of the SDI+ algorithm on an Intel Core i5 with 2.7 GHz and 8 GB RAM, running OS X Yosemite operating system. The reported execution times are low enough for the adoption of SDI+ in the dermatologist routine practice, while high throughput screening of thousands of dermoscopic images can be efficiently achieved by a straightforward GPU parallel implementation.

D. Qualitative Analysis

In the following, we qualitatively analyze some of the results achieved by the SDI+ algorithm on the ISIC dataset, highlighting its advantages and disadvantages.

To stress the importance of the preliminary information extraction step, we compare SDI+ results with those computed by the same algorithm, but in the whole image domain (i.e., without excluding dark areas, nor inpainting highlights and hair areas). Some examples are reported in Fig. 10. Here, we show that dark areas around the images should be appropriately considered to exclude them by the segmentation mask (e.g., first row, columns (f)–(g)). Moreover, highlights should be carefully taken into account to avoid affecting the automatic choice of the segmentation thresholds (e.g., last row, columns (f)–(g)). Finally, also hair can severely confound the segmentation process, as it connects different CCs (e.g., second row, columns (f)–(g)).

In Section II-B1 and in all the examples previously reported, we have shown that either *Rnorm* or *Vcompl* (sometimes both) allow a proper segmentation of the skin lesion based on automatic thresholding. However, there are cases where neither of the two can identify the correct lesion candidate. This is exemplified in Fig. 11, showing a lesion having a color very similar to the skin color, that prevents the automatic choice of a single suitable segmentation threshold. Multi-thresholding could be considered to solve these cases (e.g., [38]).

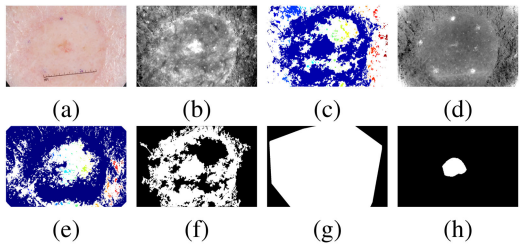

Fig. 11. Analysis of color bands: (a) ISIC dataset image 15958; (b) *Rnorm* band; (c) CCs in *Rnorm* segmentation; (d) *Vcompl* band; (e) CCs in *Vcompl* segmentation; (f) selected CC; (g) final SDI+ segmentation; (h) ground truth.

Often, SDI+ can handle some confounding artifacts frequently found in dermoscopic images, such as ink marker signs, since the selection of the image ROI partly succeeds in excluding them (see Section II-A and last column of Fig. 1). Moreover, the combined use of *Rnorm* and *Vcompl* bands can help handling ink pixels that erroneously remain in the ROI, that could still affect the segmentation. Examples are reported in Fig. 12, showing that the ink marker signs that remain into the ROI are selected as the best lesion candidate in *Vcompl* [Fig. 12(f)], but not in *Rnorm* [Fig. 12(d)]. Discarding them from the final result depends upon the segmentation selection phase, which can succeed or not [first and second rows of Fig. 12(g), respectively], based on the satisfaction of the adopted selection criteria. These observations suggest that explicitly addressing these artifacts in the first two steps of SDI+ could lead to increased accuracy and to the exploitation of the prior knowledge they represent. This holds true also for other confounding artifacts, such as color calibration charts.

Finally, we observe that, although most of the times the convex hull of the initial SDI+ segmentation better conforms to the ground truth (see Section II-C), it can erroneously in-

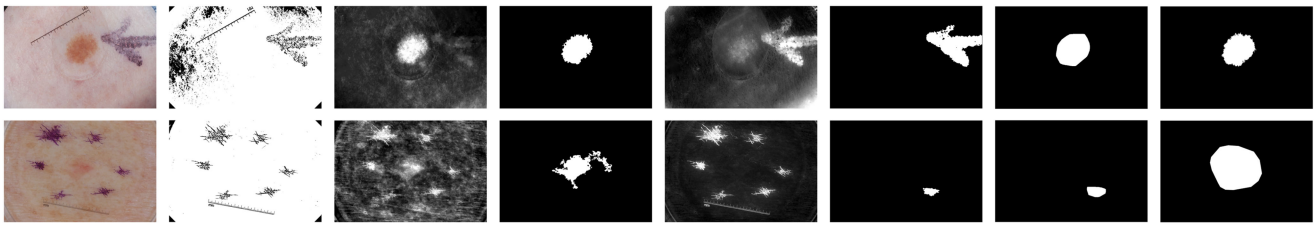

Fig. 12. Handling ink marker signs: (a) ISIC dataset images 13216 and 13191; (b) ROI mask; (c) *Rnorm* band; (d) *Rnorm* segmented lesion; (e) *Vcompl* band; (f) *Vcompl* segmented lesion; (g) final SDI+ segmentation; (h) ground truth.

Fig. 13. Analysis of post-processing: (a) ISIC dataset image 12272; (b) initial SDI+ segmentation; (c) final SDI+ segmentation; (d) ground truth.

clude not only the lesion but also vast skin areas into the final segmentation. This is the case, for example, of Fig. 13, where the ruler mark has been erroneously included into the initial segmentation, leading to an excessively wide convex hull in the final result.

IV. Discussion and Conclusions

We proposed the SDI+ algorithm for the automatic segmentation of dark lesions in dermoscopic images. It consists of three consecutive main steps: preliminary information extraction, segmentation, and post-processing.

The first step detects dark borders and corners, specular highlights, and hair, which deserve specific treatment in lesion segmentation. It is fundamental for SDI+ and can be useful for any other lesion segmentation algorithm. We observed that the detection of other artifacts that confound the automatic segmentation, such as ink marker signs and color calibration charts, could help further improve the segmentation results.

The second step considers two color bands (*Rnorm* and *Vcompl*) which are shown to be particularly suited for segmenting dark lesions by thresholding. While dark areas are excluded from the segmentation, highlights and hair areas are preliminarily inpainted, to reduce lesion over-segmentation. The best of the two segmentations obtained in *Rnorm* and *Vcompl* is chosen according to geometric and shape features of the segmented areas, in a way that is independent of the inpainting accuracy. We observed that multi-thresholding could help solving few cases where single thresholds are inadequate for segmentation. Moreover, we provided hints on possible generalizations to cover the case of bright or non-uniformly colored, as well as multiple, lesions.

Post-processing refines the obtained binary mask, to better conform it to what is usually manually selected as lesion by the expert dermatologist. This step deserves further research to achieve even more accurate results.

Extensive experiments were carried out on the ISIC 2017 dataset, a useful and comprehensive framework to deeply test any lesion segmentation method and to easily and fairly compare it to state-of-the-art methods, thus promoting further research toward new and more accurate methods. We carried out an in-depth analysis of its images and related ground truths that we hope will help further improve the framework.

SDI+ achieves high performance on most of the dermoscopic images it has been devised for. Results are extremely accurate as compared to ground truths produced by automatic tools, much less as compared to those produced by manual labeling. Finally, execution times are low enough for the adoption of SDI+ in the dermatologist routine practice.

Acknowledgement

The work was carried out also within the activities of the authors as members of the INdAM Research group GNCS. The work of M. R. Guarracino was conducted at National Research University Higher School of Economics. The authors would like to thank the anonymous reviewers for their valuable comments and G. Trerotola for the technical support.

References

[1] H. Rogers *et al.*, "Incidence estimate of nonmelanoma skin cancer (keratinocyte carcinomas) in the US population, 2012," *JAMA Dermatol.*, vol. 151, no. 10, pp. 1081–1086, 2015.

[2] "Cancer in Australia 2017," 2017. [Online]. Available: http://www.aihw.gov.au/publication-detail/?id=60129558547

[3] "Surveillance epidemiology, and end results program," National Cancer Institute, Rockville, MD, USA, 2017. [Online]. Available: http://seer.cancer.gov/

[4] W. Stolz *et al.*, "ABCD rule of dermoscopy: A new practical method for early recognition of malignant melanoma," *Eur. J. Dermatol.*, vol. 4, pp. 521–527, 1994.

[5] M. Burroni *et al.*, "Melanoma computer aided diagnosis: Reliability and feasibility study," *Clin. Cancer Res.*, vol. 10, pp. 1881–1886, 2004.

[6] V. Cozza, M. R. Guarracino, L. Maddalena, and A. Baroni, "Dynamic clustering detection through multi-valued descriptors of dermoscopic images," *Statist. Med.*, vol. 30, no. 20, pp. 2536–2550, 2011.

[7] M. E. Celebi *et al.*, "A methodological approach to the classification of dermoscopy images," *Comput. Med. Imag. Graph.*, vol. 31, no. 6, pp. 362–373, 2007.

[8] M. E. Celebi, G. Schaefer, H. Iyatomi, and Stoecker, "Lesion border detection in dermoscopy images," *Comput. Med. Imag. Graph.*, vol. 33, no. 2, pp. 148–153, 2009.

[9] I. Maglogiannis and C. N. Doukas, "Overview of advanced computer vision systems for skin lesions characterization," *IEEE Trans. Inf. Technol. Biomed.*, vol. 13, no. 5, pp. 721–733, Sep. 2009.

[10] E. Celebi, Q. Wen, S. Hwang, H. Iyatomi, and G. Schaefer, "Lesion border detection in dermoscopy images using ensembles of thresholding methods," *Skin Res. Technol.*, vol. 19, no. 1, pp. e252–e258, 2013.

[11] F. Peruch, F. Bogo, M. Bonazza, V. M. Cappelleri, and E. Peserico, "Simpler, faster, more accurate melanocytic lesion segmentation through MEDS," *IEEE Trans. Biomed. Eng.*, vol. 61, no. 2, pp. 557–565, Feb. 2014.

[12] M. E. Celebi, T. Mendonca, and J. S. Marques, *Dermoscopy Image Analysis*. Boca Raton, FL, USA: CRC Press, 2015.

[13] M. E. Celebi, Q. Wen, H. Iyatomi, K. Shimizu, H. Zhou, and G. Schaefer, "A state-of-the-art survey on lesion border detection in dermoscopy images," in *Dermoscopy Image Analysis*. Boca Raton, FL, USA: CRC Press, 2015, pp. 97–129.

[14] B. Bozorgtabar, M. Abedini, and R. Garnavi, "Sparse coding based skin lesion segmentation using dynamic rule-based refinement," *Machine Learning in Medical Imaging*. New York, NY, USA: Springer, 2016, pp. 254–261.

[15] Z. Ma and J. M. R. S. Tavares, "A novel approach to segment skin lesions in dermoscopic images based on a deformable model," *IEEE J. Biomed. Health Inf.*, vol. 20, no. 2, pp. 615–623, Mar. 2016.

[16] N. C. F. Codella, *et al.*, "Skin lesion analysis toward melanoma detection: A challenge at the 2017 international symposium on biomedical imaging (ISBI), hosted by the international skin imaging collaboration (ISIC)," arXiv: 1710.05006 [cs.CV], 2017.

[17] M. R. Guarracino and L. Maddalena, "Segmenting dermoscopic images," arXiv:1703.03186 [cs.CV], 2017.

[18] A. R. Smith, "Color gamut transform pairs," *ACM SIGGRAPH Comput. Graph.*, vol. 12, no. 3, pp. 12–19, 1978.

[19] A. Madooei and M. S. Drew, "Detecting specular highlights in dermatological images," in *Proc. 2015 IEEE Int. Conf. Image Process.*, 2015, pp. 4357–4360.

[20] A. Artusi, F. Banterle, and D. Chetverikov, "A survey of specularity removal methods," *Comput. Graph. Forum*, vol. 30, no. 8, pp. 2208–2230, 2011.

[21] F. Torres, J. Angulo, and F. Ortiz, "Automatic detection of specular reflectance in colour images using the MS diagram," in *Computer Analysis of Images and Patterns*. New York, NY, USA: Springer, 2003, pp. 132–139.

[22] L. Ballerini, R. B. Fisher, B. Aldridge, and J. Rees, "A color and texture based hierarchical K-NN approach to the classification of non-melanoma skin lesions," in *Color Medical Image Analysis*. Dordrecht, the Netherlands: Springer, 2013, pp. 63–86.

[23] T. Lee, V. Ng, R. Gallagher, A. Coldman, and D. McLean, "Dullrazor: A software approach to hair removal from images," *Comput. Biol. Med.*, vol. 27, no. 6, pp. 533–543, 1997.

[24] F.-Y. Xie, S.-Y. Qin, Z.-G. Jiang, and R.-S. Meng, "PDE-based unsupervised repair of hair-occluded information in dermoscopy images of melanoma," *Comput. Med. Imag. Graph.*, vol. 33, no. 4, pp. 275–282, 2009.

[25] Q. Abbas, M. Celebi, and I. F. Garcia, "Hair removal methods: A comparative study for dermoscopy images," *Biomed. Signal Process. Control*, vol. 6, no. 4, pp. 395–404, 2011.

[26] Q. Abbas, I. F. Garcia, M. E. Celebi, and W. Ahmad, "A feature-preserving hair removal algorithm for dermoscopy images," *Skin Res. Technol.*, vol. 19, no. 1, pp. e27–e36, 2013.

[27] Y. George, M. Aldeen, and R. Garnavi, "Skin hair removal for 2d psoriasis images," in *Proc. 2015 Int. Conf. Digit. Image Comput.: Techn. Appl.*, 2015, pp. 1–8.

[28] J. Koehoorn *et al.*, "Efficient and effective automated digital hair removal from dermoscopy images," *Math. Morphol.-Theory Appl.*, vol. 1, no. 1, pp. 1–17, 2016.

[29] N. K. Mishra and M. E. Celebi, "An overview of melanoma detection in dermoscopy images using image processing and machine learning," arXiv:1601.07843 [cs.CV], 2016.

[30] R. Garnavi, M. Aldeen, M. E. Celebi, G. Varigos, and S. Finch, "Border detection in dermoscopy images using hybrid thresholding on optimized color channels," *Comput. Med. Imag. Graph.*, vol. 35, no. 2, pp. 105–115, 2011.

[31] C. Barata, M. E. Celebi, and J. S. Marques, "Improving dermoscopy image classification using color constancy," *IEEE J. Biomed. Health Inf.*, vol. 19, no. 3, pp. 1146–1152, May 2015.

[32] N. Otsu, "A threshold selection method from gray-level histograms," *IEEE Trans. Syst., Man, Cybern.*, vol. 9, no. 1, pp. 62–66, Jan. 1979.

[33] S. Drew, C. Chubb, and G. Sperling, "Precise attention filters for weber contrast derived from centroid estimations," *J. Vision*, vol. 10, 2010, Art. no. 20.

[34] M. Guarracino and L. Maddalena, "SDI+: A novel algorithm for segmenting dermoscopic images," 2017. [Online]. Available: http://www.na.icar.cnr.it/ maddalena.l/SDIplus.html

[35] A. Bono *et al.*, "The ABCD system of melanoma detection: A spectrophotometric analysis of the asymmetry, border, color, and dimension," *Cancer*, vol. 85, no. 1, pp. 72–77, 1999.

[36] D. Gutman *et al.*, "Skin lesion analysis toward melanoma detection: A challenge at the International Symposium on Biomedical Imaging (ISBI) 2016, hosted by the International Skin Imaging Collaboration (ISIC)," arXiv:1605.01397 [cs.CV], 2016.

[37] Y. Yuan, "Automatic skin lesion segmentation with fully convolutional-deconvolutional networks," arXiv:1703.05165 [cs.CV], 2017.

[38] G. Lee, O. Lee, J. Kim, J. Moon, and C. Oh, "Dermoscopy image assessment based on perceptible color regions," in *Dermoscopy Image Analysis*. Boca Raton, FL, USA: CRC Press, 2015,pp. 231–246.